Breath of impact: Unveiling the dynamics of exhalation-driven deposition of polydisperse particles in lung across varied physical activities

Muhammad Farrukh Mehmood [a], Adnan Munir [a], Umar Farooq [a,b], Hafiz Hamza Riaz [a], Ming Zhao [c,*], Mohammad S. Islam [d]

[a] School of Mechanical and Manufacturing Engineering, National University of Sciences and Technology, H-12 Islamabad, Pakistan
[b] Department of Mechanical and Computer-Aided Engineering, National Formosa University, Yunlin 632, Taiwan, PR China
[c] School of Engineering, Design and Built Environment, Western Sydney University, Penrith 2751, NSW, Australia
[d] School of Mechanical and Mechatronic Engineering, University of Technology Sydney, Ultimo, NSW 2007, Australia

HIGHLIGHTS

- Analysis of exhalation-driven deposition informs pollutant health risks.
- Active physical conditions increase deposition.
- Deposition comparison of fine (PM2.5) and coarse (PM2.5–10) particles.
- High density particles influence lungs health more.
- Gravity impact: strong at low flow, weak at high flow when normal to gravity.

GRAPHICAL ABSTRACT
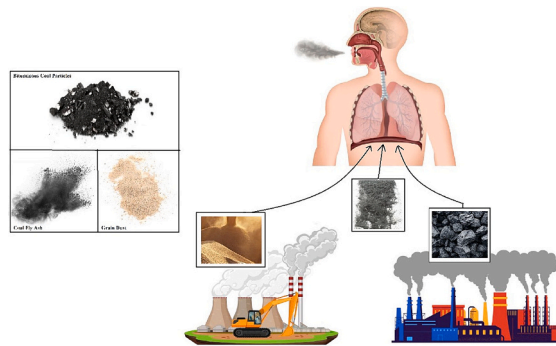
ABSTRACT

Continuous deposition of workplace pollutant particles on lung airways during respiratory actions seriously threatens the lung health of persons performing tasks in polluted environments. This study aims to analyze the exhalation-driven deposition of fine and coarse occupational pollutant particles in polydisperse form. Computer simulations are conducted to study the patterns of deposition of grain dust, coal fly ash, and bituminous coal particles. Key findings include the observation of early emergence of secondary flows in the real model, a notable shift in deposition patterns towards the post-bifurcation zones, and influence of physical activity intensity on particle deposition. Additionally, deposition primarily occurs near cranial ridge during inhalation, while exhalation leads to deposition in pre- and post-bifurcation zones. PM2.5 deposition is minimal and random in idealized model but becomes more significant and consistent in real model. This research underscores the increased risk of lung diseases for workers in polluted environments during vigorous activity.

* Corresponding author.
  E-mail address: M.Zhao@westernsydney.edu.au (M. Zhao).

1. Introduction

The Industrial Revolution instigated the atmosphere to be filled with various harmful pollutants. Almost 99 % of the world's population resides in areas where air pollution exceeds the limit and approximately 7 million people die prematurely each year because of atmospheric contamination [44]. In addition, occupational pollution has become a grave concern that causes lung cancer and cardiovascular diseases [27]. Paul et al. [28] found that 18.3 % of the deaths of coal miners due to Coal Worker's Pneumoconiosis (CWP) were caused by the inhalation of coal dust. Epidemiological studies have found grain-induced asthma to be a prevalent disease in grain processing facilities ([33,41]. Coal fly ash (CFA), a waste product of thermal power plants, is widely used for making bricks [10]. Professionals in CFA-related industries are at serious health risk because CFA contains carcinogenic constituents such as lead and arsenic [48].

Air pollution at coal mines (CM), grain processing facilities (GPF), and coal fly ash brick industry (CFBI) is referred to as "particulate matter (PM)" pollution [8,17,42]. The most common two types of PM, based on the size of particles, are PM2.5 (diameter < 2.5 μm) and PM2.5–10 (diameter between 2.5 and 10 μm), which are also called fine and coarse PM respectively [25]. These particles are brought into the lungs during the respiratory process and deposit on different parts of lung airways [13,22]. The elevated mortality rates associated with PM2.5 and PM2.5–10-induced lung diseases have been documented in studies by Janssen et al. [18] and Lu et al. [23].

Physical activities (PA) in working environments with particulate matter pollution further escalate the risk of uptake and deposition of pollutant particles within the lung airways [12]. The relationship between physical activity levels in different polluted environments and particle deposition is not fully understood [11]. Most of the studies on the impact of pollutant particles on lung health focus on inhalation only. Particle deposition efficiency (DE) is defined as the proportion of particles deposited within the system compared to the total number of particles that entered the system. Deposition efficiency increases with an

increase in particle size and physical activity intensity in the trachea and first three generations (G1-G3) [37]. A similar trend of deposition efficiency is observed in G3-G5, but it is found to decrease in lower airways (G14-G16) with the increase in PA intensity [6]. Research regarding the influence of exhalation on the deposition of these particles during various levels of PA is rare. In an experimental study on exhalation, Kim et al. [19] found deposition hot spots in the pre-bifurcation zone of G3-G4 and attributed this phenomenon to the vortices generated by the secondary flows. Balásházy & Hofmann [2] also found similar patterns of deposition hotspots in their numerical study on particle deposition in expiratory flow. Longest & Vinchurkar [21] observed the correlation between particle deposition during exhalation and Dean number (D) and found the deposition efficiency to increase when D > 100 at a constant Stokes number. All these researchers relied on idealized airway structure. Given the intricacy brought about by variances in airway anatomy among people, the necessity for study on real geometries becomes clear. Studies have investigated the impact of external fields on inhalation driven particle deposition in real lung model, with findings showing that magnetic fields can enhance deposition efficiency by affecting particle behavior based on size and field strength [30,31]. Acoustically-driven techniques have revealed that variations in acoustic parameters and resonance conditions significantly influence particle deposition efficiency in targeted regions [29]. Moreover, various studies have reported their findings on pollutant inhalation during the inhalation phase of the breathing cycle [35]. However, studies analyzing the inhaled pollutant behavior during the exhalation phase are lacking in the current literature.

Based on granularity, micro particles are categorized as PM2.5 (fine) and PM10 (coarse). Research shows that high concentrations of pollutant particles of PM2.5 category can damage nasal epithelium, impair mucociliary clearance, and exacerbate respiratory conditions such as allergic rhinitis [45]. Exposure to trace metals in PM10, particularly cadmium and cobalt, poses significant health risks, including elevated cancer and cardiovascular disease risks, with the child population being especially vulnerable [4]. Pollutant particles are
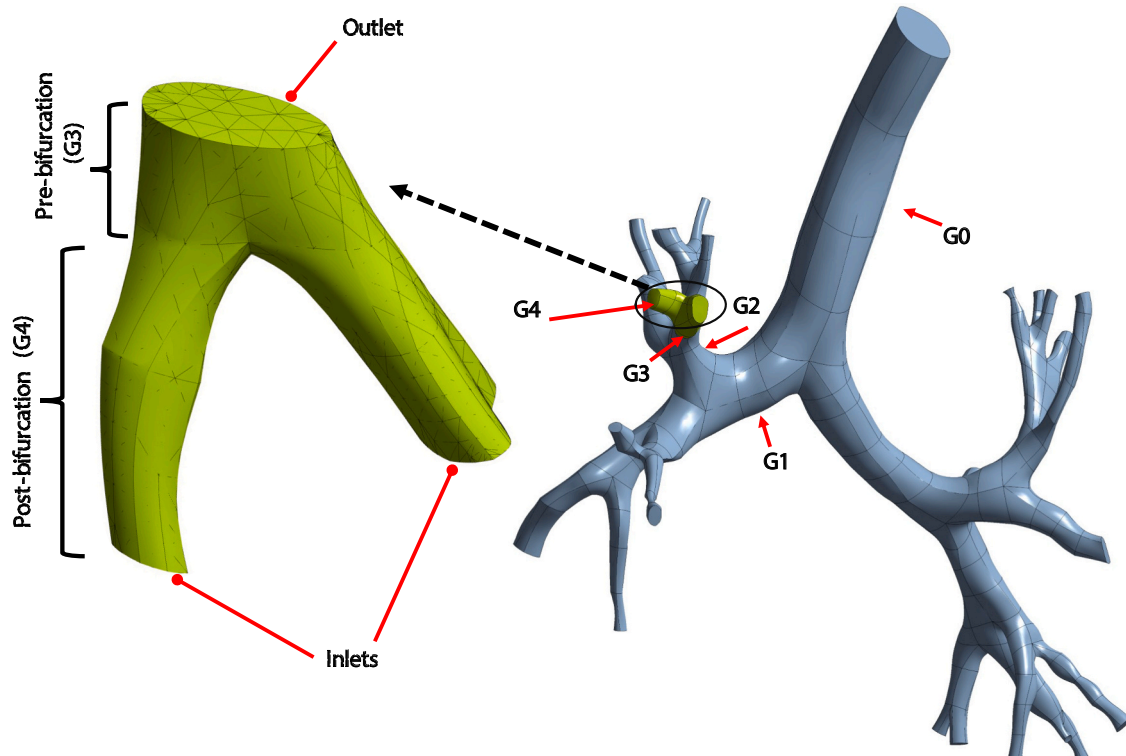

Fig. 1. Real lung model: (Right) CT-scanned lung model encompassing the trachea to generation 4; (Left) Extracted segment showing generations 3 and 4.
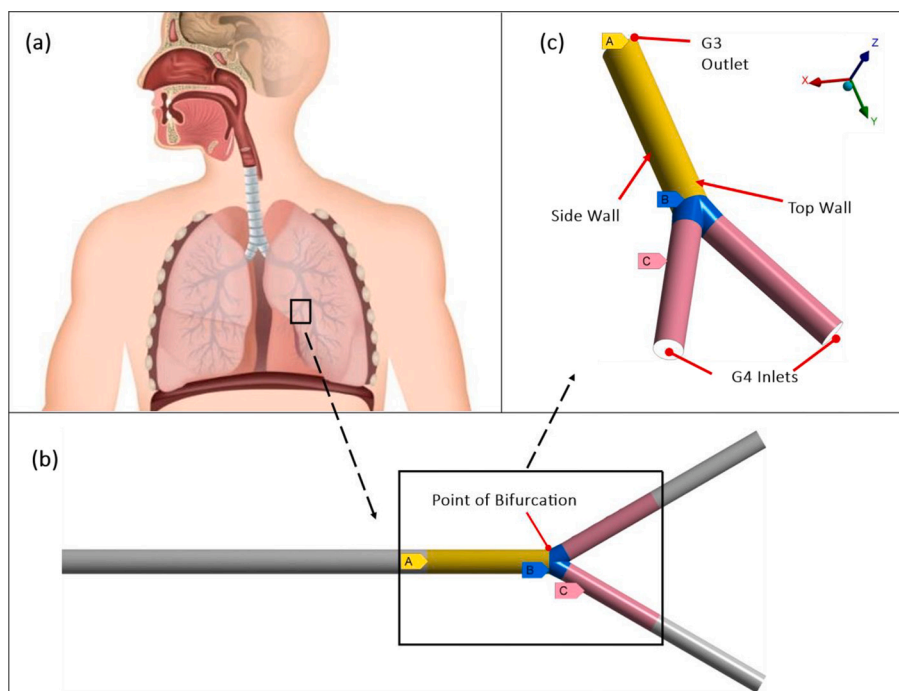
Fig. 2. (a): Respiratory tract in the human body. (b): Schematic diagram of G3-G4. Colored section 'A' represents pre-bifurcation zone and sections 'B', and 'C' post-bifurcation zone. (c): The orientation of G3-G4 human lung airway with inlets, outlet, top and side walls indicated.

found with a wide range of diameters. However, most of the researchers have focused on monodispersed particle deposition in their studies. Only a few studies have analyzed the polydisperse particle deposition [15]. Musante et al. [26] studied the effect of the density and particle size along with polydispersity on the DE and found that large but light particles deposited less than tiny but dense particles. However, the difference in deposition efficiencies becomes less prominent with an increase in median diameter. In a comparison reported by Cui et al. [5], the deposition efficiency (DE) of polydisperse particles was higher than that of monodisperse particles. Turbulence effects on the deposition of large-size particles are found to be higher than on small-size particles in a polydisperse transport and deposition (TD) study [16]. All these researchers considered inhalation to study the polydisperse deposition. Recent studies reveal that exhalation activities and indoor conditions significantly impact virus deposition in the respiratory tract, with speaking causing nearly double the deposition compared to breathing [24]. The study finds that large particles predominantly deposit in the upper airway during inhalation, while fine particles exhibit a notable deposition during exhalation [3]. No existing studies have examined the influence of polydispersity on aerosol deposition in bronchial airways during exhalation.

This study aims to investigate the polydisperse deposition of pollutant particles on the G3-G4 pulmonary airways in the context of workplace pollution under four levels of physical activities: sedentary state (SS), light activity (LA), moderate activity (MA), and vigorous activity (VA). G3-G4 is selected because we can test our numerical model at this bifurcation using experimental data [19]. We shall analyze both ideal and real lung models and provide a comparison between the two scenarios. Work activities may involve bending or lying positions of body, making the gravity direction $\vec{g}$ perpendicular to all the G3-G4 airways as indicated in Fig. 2c. As the sedimentation due to gravity enhances particle deposition, we considered the configuration shown in Fig. 2c to examine the maximum possible deposition rates.

The typical corresponding flow rates at the tracheal outlet for SS, LA, MA, and VA activities are 15 l/min, 30 l/min, 45 l/min, and 60 l/min respectively ([2,6,37]. The pollutants within three distinct working environments, including grain dust (GD) in GPFs, coal fly ash (CFA) in

CFBIs, and bituminous coal (BC) in CMs, are the focus of the study. These pollutants possess different chemical compositions which are characterized in this study by respective bulk densities (GD: 400 kg/m^3, CFA: 1120 kg/m^3, BC: 1340 kg/m^3 [7,36,40]. The polydispersity of the particles is considered for both PM2.5 and PM2.5–10, with ten diameters for each category.

Building on the insights gained from the literature analysis, we formulate a hypothesis that considering particle polydispersity and expiratory flow, the deposition of polydisperse particles during exhalation is higher compared to monodisperse particles.

2. Numerical model

2.1. Airway geometry

The CT-scanned DICOM images capturing the lung of a 55-year-old adult are obtained from a local hospital. Utilizing geometry modeling software, a three-dimensional lung model is constructed from these images, incorporating the trachea and the first four lung generations (G0-G4). For the present study, a segment of the lung model spanning generations G3 to G4 is extracted (Fig. 1).

The idealized 3D model of G3-G4 airways is constructed by taking the dimensions as per the experimental model of Kim et al. [19]. The diameters of G3 and G4 airways are 0.5 cm and 0.4 cm, respectively [43], and the respective lengths are 10 cm and 5 cm, respectively. The point of bifurcation is defined as the point where the G3 airway splits into two parts. The focus of the analysis is between the region 2.5 cm before the bifurcation point and 2.5 cm after the bifurcation point as indicated in the colored part in Fig. 2b. The region is sub-divided (as seen in Fig. 2b and c.) into two zones: Pre-bifurcation zone and post-bifurcation zone, in correspondence with sections C and D of experimental model of [19].

2.2. Governing equations of airflow and particle dynamics

ANSYS Fluent is used to conduct numerical analysis. The flow is assumed to be incompressible and transient. The solver solves the
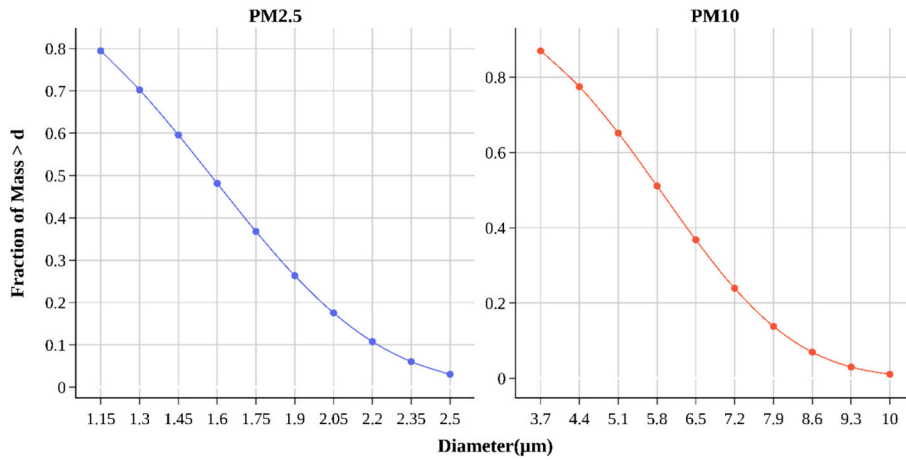
Fig. 3. Initial mass distribution of polydisperse particles.

Reynolds Averaged Navier-Stokes (RANS) equations to simulate the air flow in the computational domain. The RANS equations are given below:

$$\frac{\partial}{\partial x_i}(\rho u_i) = 0 \tag{1}$$

$$\frac{\partial}{\partial t}(\rho u_i) + \frac{\partial}{\partial x_j}(\rho u_i u_j) = -\frac{\partial p}{\partial x_i} + \frac{\partial}{\partial x_j}\left[\mu\left(\frac{\partial u_i}{\partial x_j} + \frac{\partial u_j}{\partial x_i}\right)\right] + \frac{\partial}{\partial x_j}\left(-\rho\,\overline{u_i' u_j'}\right) \tag{2}$$

where i ranges from 1 to 3, $(x_1, x_2, x_3) = (x, y, z)$, ρ and μ are the density and molecular viscosity of air respectively, g is the gravitational acceleration in the z-direction, and 'u_i' represents the three-dimensional velocity in the x_i-direction and $-\rho\,\overline{u_i' u_j'}$ is Reynolds stress term which is given as:.

$$-\rho\,\overline{u_i' u_j'} = \mu_t\left(\frac{\partial u_i}{\partial x_j} + \frac{\partial u_j}{\partial x_i} - \frac{2}{3}\frac{\partial u_k}{\partial x_k}\delta_{ij}\right) - \frac{2}{3}\rho k\delta_{ij} \tag{3}$$

where μ_t represents turbulent eddy viscosity. δ_{ij} is the Kronecker delta, which is 1 if $i = j$ and 0 otherwise.

The Shear-Stress Transport (SST) $k - \omega$ turbulence model is employed to simulate turbulence, as it is particularly effective in handling adverse pressure gradients. This model is a refinement of the standard $k - \omega$ model, designed to offer a robust and accurate formulation in near-wall regions while maintaining independence from free-stream effects in far-field areas. The SST $k - \omega$ turbulence model, incorporating essential blending functions, is represented by the following equations:

$$\frac{\partial}{\partial t}(\rho k) + \frac{\partial}{\partial x_1}(\rho k u_1) = \frac{\partial}{\partial x_2}\left(\Gamma_k\frac{\partial k}{\partial x_2}\right) + \widetilde{G}_k - Y_k \tag{4}$$

$$\frac{\partial}{\partial t}(\rho \omega) + \frac{\partial}{\partial x_1}(\rho \omega u_1) = \frac{\partial}{\partial x_2}\left(\Gamma_\omega\frac{\partial \omega}{\partial x_2}\right) + \widetilde{G}_\omega - Y_\omega \tag{5}$$

In Eqs. (4) and (5), Γ_k and Γ_ω denote the effective diffusivity of turbulent kinetic energy (k) and dissipation rate (ω), respectively. $\widetilde{G}_k$ signifies the production of turbulent kinetic energy (k), while $\widetilde{G}_\omega$ represents the production of the specific dissipation rate (ω). Additionally, Y_k and Y_ω correspond to the dissipation of turbulent kinetic energy and the dissipation rate, respectively.

Pressure-based solver is opted to compute the incompressible flow. To simulate the motion of the particles in the Lagrangian scheme and airflow in the Eulerian scheme, the Discrete Phase Model (DPM) is used with implicit formulation. The phase coupled SIMPLE method is employed for pressure-velocity coupling while the first-order upwind scheme is used for the spatial discretization of momentum, volume fraction, and turbulent kinetic energy. To solve pressure, the PRESTO scheme is used. To model the turbulent dispersion of particles, stochastic tracking method is used with Discrete Random Walk Models (DRWM) enabled. Random Eddy Lifetime (REL) method is employed to randomize the characteristic lifetime of eddies.

The deposition mechanisms for fine and coarse are primarily gravitational sedimentation and inertial impaction [34,46]. The numerical model includes Euler-Lagrange approach with one way coupling. The path of particles is governed by the following force balance equations:

$$m_p\frac{d\boldsymbol{u}^p}{dt} = \boldsymbol{F}_{body} + \boldsymbol{F}_{surface} \tag{6}$$

here m_p and $\boldsymbol{u}^p$ respresent the mass of particle and its velocity vector respectively. $\boldsymbol{F}_{body}$ is the gravitational force given as:

$$\boldsymbol{F}_{body} = \boldsymbol{F}_{gravitational} = m_p\frac{(\rho_p - \rho)}{\rho}\boldsymbol{g} \tag{7}$$

where ρ_p and ρ denote the densities of particle and air, respectively. $\boldsymbol{F}_{surface}$ is composed of drag force and Saffman lift force as:

$$\boldsymbol{F}_{surface} = \boldsymbol{F}_{drag} + \boldsymbol{F}_{saffman} \tag{8}$$

$$\boldsymbol{F}_{drag} = m_p\frac{\boldsymbol{u} - \boldsymbol{u}_p}{\tau} \tag{9}$$

where $\boldsymbol{u}$ denotes velocities vector air, and τ is the particle relaxation time which is given as [9]:

$$\tau = \frac{4\rho_p d_p^2}{3\mu C_d Re_p} \tag{10}$$

here the paprameters d_p and C_d are the particle diameter and drag cofficient respectively. Re_p represents the particle Reynolds number relative to air velocity given as:

$$Re_p = \frac{\rho d_p}{\mu}\left|\boldsymbol{u}_p - \boldsymbol{u}\right| \tag{11}$$

Saffman's Lift force is given as[20,38]:

$$\boldsymbol{F}_{Saffman} = m_p\frac{2K\nu^{\frac{1}{2}}\rho d_{ij}(\boldsymbol{u} - \boldsymbol{u}_p)}{\rho_p d_p(d_{lk}d_{kl})^{\frac{1}{4}}} \tag{12}$$

where ν is kinematic viscosity, $K = 2.594$ is the coefficient of Saffman's Lift force, $d_{ij} = \frac{1}{2}(u_{i,j} + u_{j,i})$ is the deformation rate tensor, and $(d_{lk}d_{kl})^{\frac{1}{4}}$ is a measure of the turbulence intensity, derived from the Reynolds stresses or turbulence tensor components.
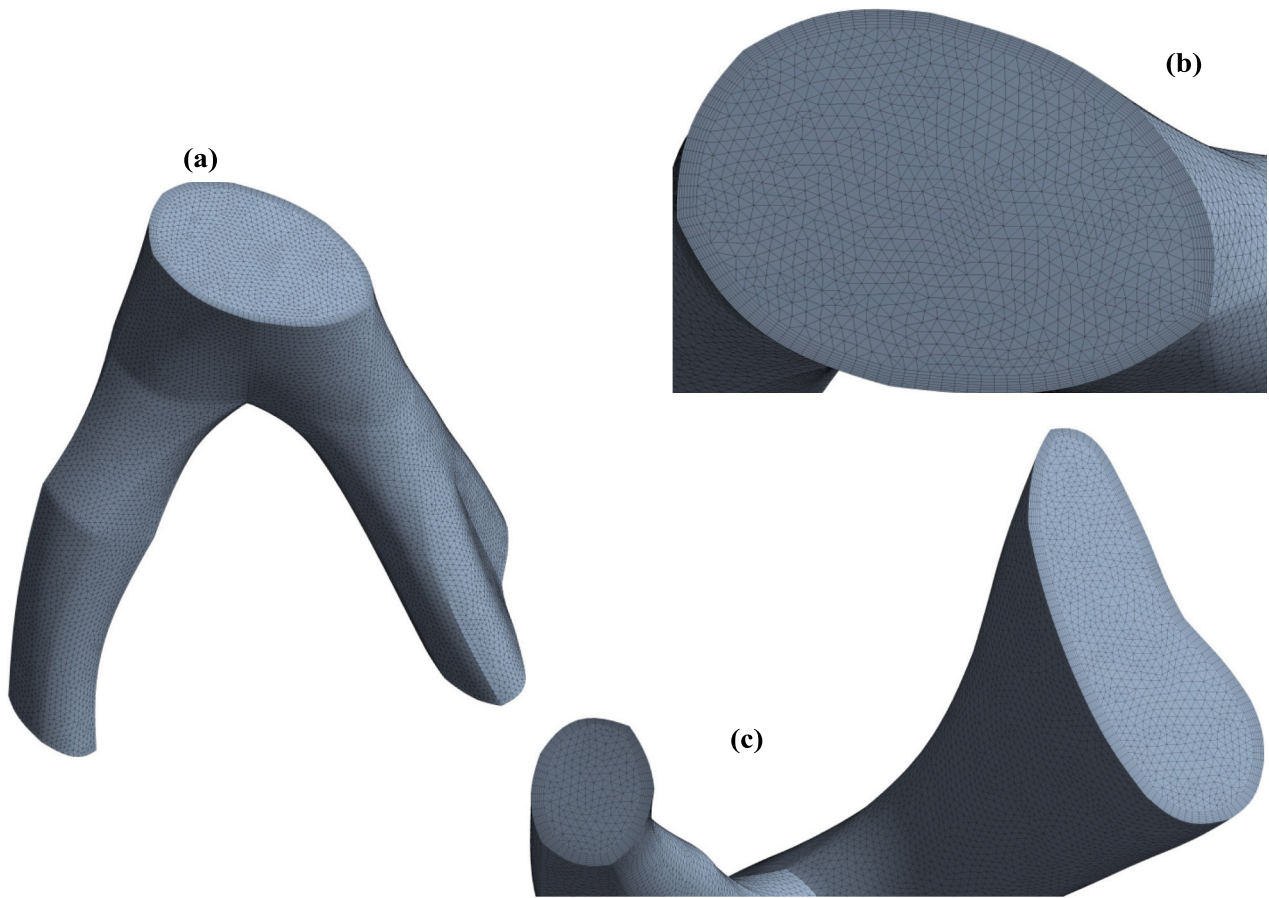
Fig. 4. Unstructured mesh representation of the G3-G4 real geometry model with 7 inflation layers: (a) Full model mesh, (b) Outlet mesh, and (c) Inlet mesh.

The exact number of particles that enters G4 during exhalation cannot be known without a whole lung analysis [14]. In this study the percentage of particles that are deposited in the G3-G4 bifurcation zone is analyzed and for each numerical case, 44,370 particles are used. The numbers of 44,730 and 61,040 particles for ideal and real lung geometries, respectively, are chosen based on particle independence tests. The diameters chosen for the study range from 1.15 μm to 2.5 μm for PM2.5 and from 3.7 μm to 10 μm for PM2.5–10. Initial distribution of diameters is based on Rosin-Rammler size distribution method [39,47]. According to this distribution method, mass fraction of particles greater than a diameter *d*, as shown in Fig. 3, is given by following equation [1]:

$$Y_d = e^{-\left(\frac{d}{\bar{d}}\right)^n} \tag{13}$$

where $\bar{d}$ is size constant with a value of 1.75 μm or PM2.5 and 6.5 μm for PM2.5–10 and *n* is the spread parameter, which has value of 3.5.
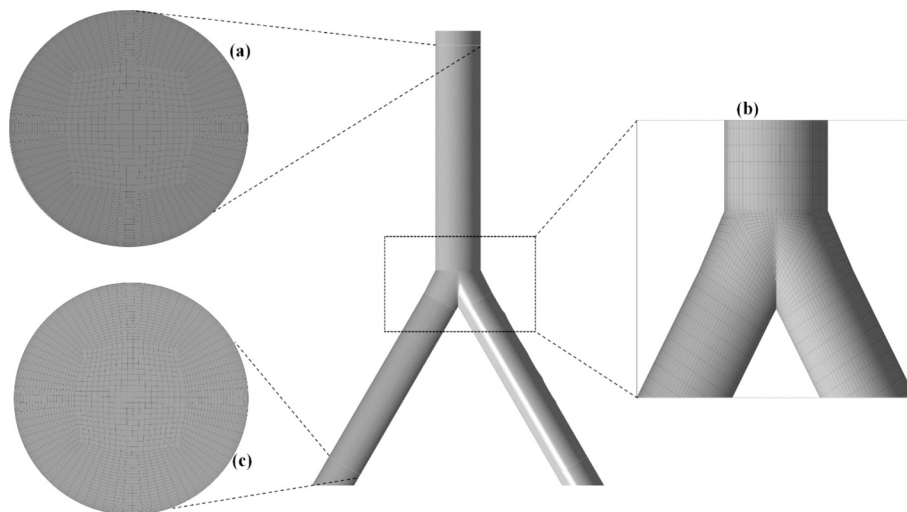

Fig. 5. Structured mesh representation of the ideal model for G3-G4 with 25 inflation layers: (a) Outlet mesh, (b) Mesh in the vicinity of the bifurcation, and (c) Inlet mesh.
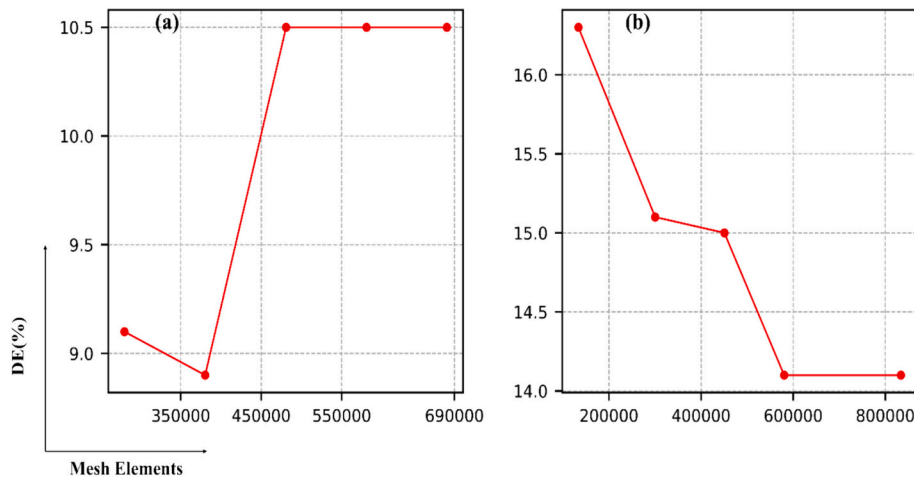
Fig. 6. Results of mesh independence tests conducted with the particles of 5 μm diameter are depicted in (a) for ideal model mesh and (b) for real model mesh.

2.3. Boundary conditions

During exhalation, the air enters the lung model reversely at the two openings of G4 which act as inlets for the air flow. For this study, a velocity-inlet boundary condition is employed at these inlets. The inlet velocity is specified based on the different physiological with the Reynolds numbers set to 332, 664, 994, and 1327, corresponding to tracheal outflows of 15 lpm, 30 lpm, 45 lpm, and 60 lpm, respectively. The single opening of G3 acts as outlet for the reverse air flow. A zero-gauge pressure boundary condition is employed at this location.

Particles are introduced at G4 inlets using a surface injection setup with the initial velocities matching the inlet airflow velocities. To simulate mucosal action of particle deposition, trap boundary condition is implemented at the model walls. An escape boundary condition is implemented at the outlet face of G3, allowing the non-deposited particles to exit the computational domain with the airflow.

2.4. Deposition fraction

The deposition fraction is analyzed in two ways:

a) Deposition of individual particles diameters based on their initial distribution.

$$DE_x = \frac{N_{trap,x}}{N_{inj,x}} \times 100 \tag{14}$$

where $N_{inj,x}$ and $N_{trap,x}$ represent the number of particles of a diameter x injected into the system and trapped by the lung walls.

b) Total deposition which refers to the cumulative deposition of particles of all diameters.

$$DE_{total} = \frac{\sum_{x=1}^{n} N_{trap,x}}{\sum_{x=1}^{n} N_{inj,x}} \times 100 \tag{15}$$

2.5. Mesh Independence and model validation with experimental data

The computational domains of real and ideal lung models are discretized in unstructured and structured meshes respectively with 7 and 25 respective inflation layers near the airway walls (Figs. 4 and 5). Mesh independence tests are performed by implementing the numerical model discussed above on 5 different meshes from coarse to fine with 5 μm particle and tracheal flow rate of 8 l/min. The difference between deposition efficiencies with the last two meshes is close to 0 % in both the cases. Thus, the benchmark for mesh independence is achieved and

Table 1
Parameter values taken from [19] for the model validation.

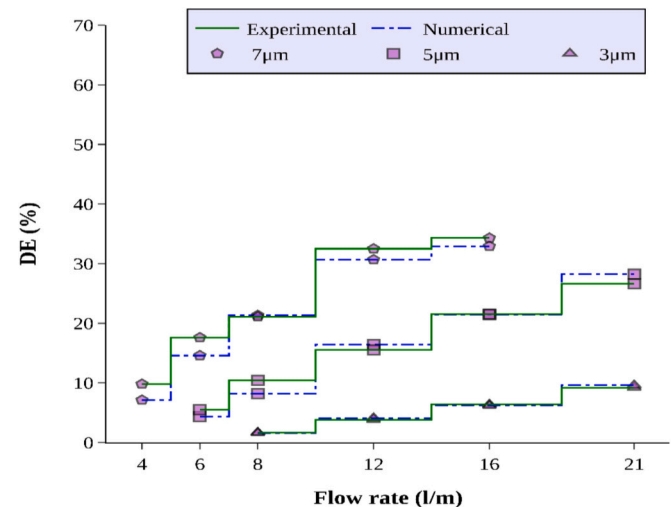| Parameter	Value
Particle material	Olefin acid
Particle Density (kg/m^3)	891
Flow rates at parent branch (l/min)	4, 6, 8, 12, 16, 21
Particle diameter (μm)	3, 5, 7

Fig. 7. Validation of numerical model for idealized lung model against the experimental data of Kim et al. [19].

meshes consisting of 580,307 elements for real geometry and 580,773 elements for ideal geometry (2nd last meshes) have been for further analyses. Results of mesh independence tests are presented in Fig. 6.

For model validation, simulations are conducted by taking the geometric dimensions and the parameters same as used in the experimental study of Kim et al. [19]. These parameters are listed in Table 1. Fig. 7 demonstrates excellent agreement between the simulated and experimentally measured deposition rates for different particle sizes during exhalation. Hence, the numerical model employed in the current study can predict highly accurate results of deposition efficiencies of various particle sizes in the upper lung generations during exhalation.
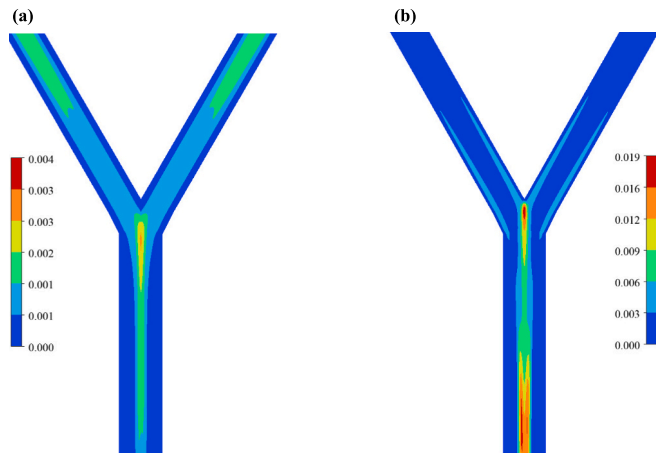
Fig. 8. Idealized model contours of normalized turbulent kinetic energy (TKE) against the inlet Reynolds numbers of, (a): 332, (b): 1327. Corresponding tracheal flow rates are 15 l/m and 60 l/m.

3. Results and discussion

3.1. Airflow analysis

In idealized airway model Reynolds numbers (Re) corresponding to tracheal outflows of 15 l/m and 60 l/m are found to be 550 and 2035 respectively at the bifurcation point of G3-G4, and 644 and 2245 respectively at the outlet of G3. Patterns of turbulent kinetic energy (TKE) normalized are shown in Fig. 8 as a measure of the turbulence formation in G3-G4 for the idealized model. Flow in G4 remains laminar for all the flow rates. At the outlet of G3, Re gains a maximum value of 644 at 15 l/min flow rate which indicates that at lower flow rates, flow remains laminar in G3 (Fig. 6a). However, at flow rate of 60 l/m (Fig. 8b), flow becomes transitional down stream of cranial ridge in G3 because Re varies from 2035 to 2245. Secondary flows develop as the air

passes through the bend section of a tube [32]. Section A in Fig. 9 lacks secondary flow vectors indicating the absence of secondary flows in G4. However, secondary flow formations are observed as flow passes through cranial ridge (cross-section B) and propagate downstream (cross-sections C and D), with the maximum strength of secondary flows occurring near the cranial ridge. Secondary flow vortices are initially generated near the top and bottom walls of the G3 (cross-section B). Their centers move towards the center of the tube and form a four-vortex flow structure at cross-sections B, C, and D. At a particular cross-section, these vortices are stronger near the top and bottom walls and weaker near the side walls.

In contrast to the idealized lung model, the real lung model exhibits the development of secondary flows in G4 even before reaching the bend at the bifurcation, as evident from sections A and B in Fig. 10. This early emergence of secondary flows can be attributed to the anatomical complexities present in real airways, such as irregularities in lung geometry, branching angles, and variations in airway diameter along the flow path. These anatomical features introduce disturbances to the airflow, prompting the formation of secondary flows. In contrast, the absence of such variations in geometric parameters in the idealized lung model results in the absence of secondary flows in G4.

3.2. Particle deposition

We first compare deposition patterns between Kim's experimental ideal lung model and our simulated real lung model. Pre- and post-bifurcation zones in our real lung model correspond to zones 'C' and 'D' respectively in Kim's paper. In contrast to Kim's ideal model, our real lung simulations reveal a notable divergence. Kim noticed deposition primarily in the pre-bifurcation zone. Contrary to Kim's findings, our real lung simulations reveal deposition principally occurring in the post-bifurcation zone instead of the pre-bifurcation zone (Fig. 11). This unexpected outcome persists across various tracheal flow rates, with deposition varying to some extent with the increase in flow rate (e.g., 90.5 % and 9.5 % at Q = 15 lpm, 86.7 % and 13.3 % at Q = 60 lpm for post and pre-bifurcation zones, respectively).
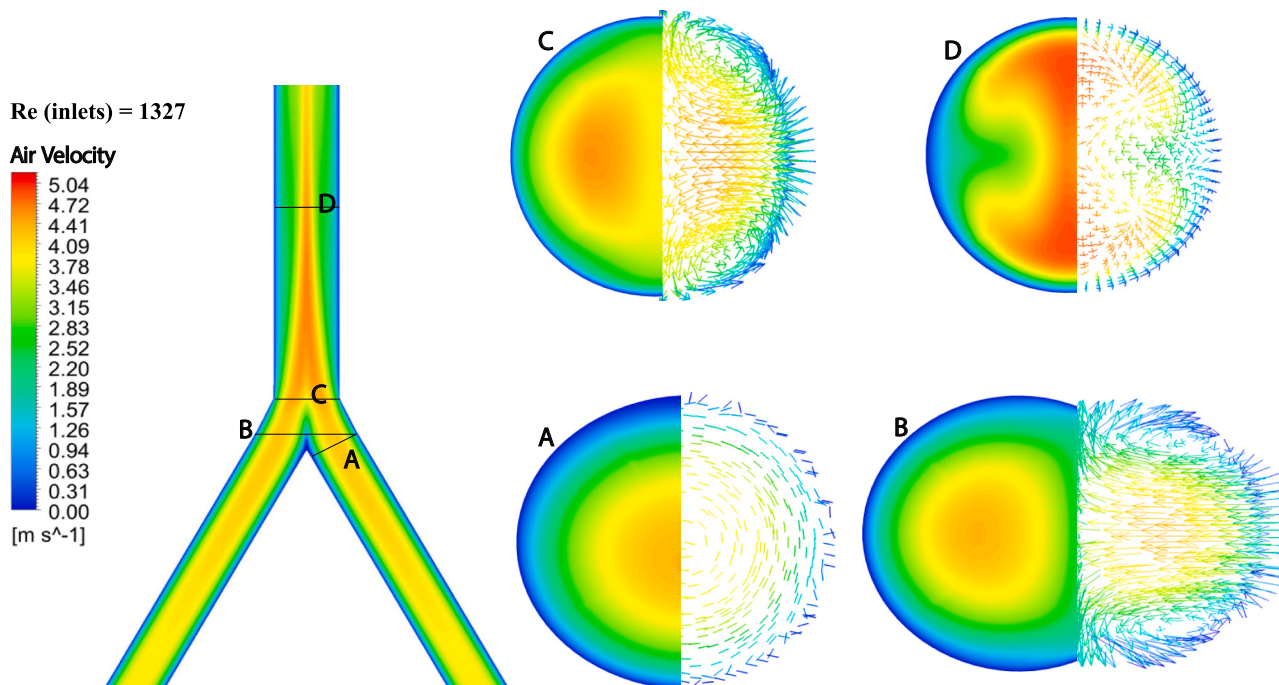

Fig. 9. Airflow patterns in the idealized G3-G4 model with inlet Reynolds number of 1327, equivalent to a tracheal flow rate of 60 l/m. Velocity contours show velocity field magnitudes, whereas velocity vectors depict secondary flow structures. Sections A, B, C, and D show upstream flow in G4 reaching the cranial ridge, flow slightly downstream of the cranial ridge, flow through the bifurcation plane, and downstream flow in G3, respectively.
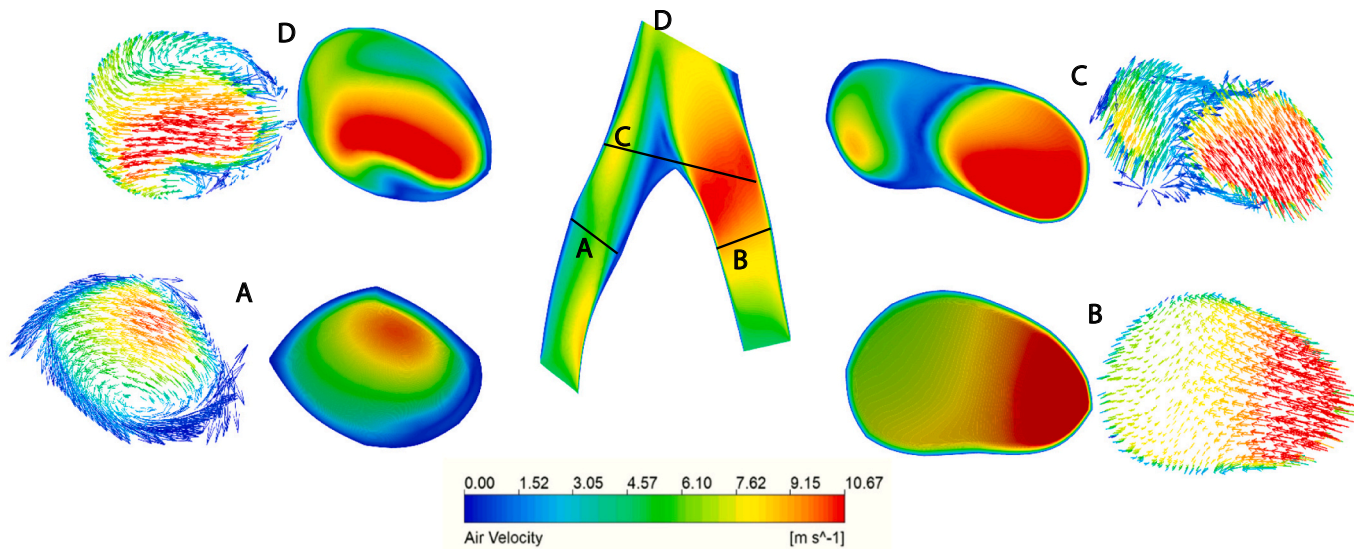
Fig. 10. Airflow patterns in the real G3-G4 model with inlet Reynolds number of 1327, equivalent to a tracheal flow rate of 60 l/m. Velocity contours show velocity field magnitudes, whereas velocity vectors depict secondary flow structures. Sections A and B depict upstream flows in G4, located away from the cranial ridge. Section C depicts flow slightly downstream of the cranial ridge, while section D shows flow through the plane of G3's output.
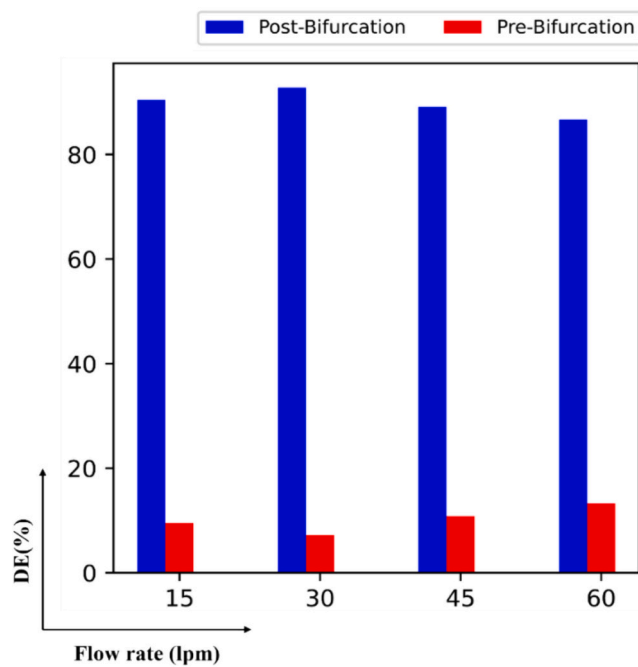

Fig. 11. Comparison of % of total deposition at post-bifurcation and pre-bifurcation zones at different levels of tracheal flow rates.

The disparity in deposition patterns between the real and idealized lung models can be attributed to the airflow dynamics illustrated in Figs. 9 and 10. Expiratory deposition is primarily influenced by the presence of secondary flows Longest & Vinchurkar [21], Kim et al. [19]. In the idealized lung model, G4 is devoid of secondary flows, resulting in minimal deposition within this region, while deposition predominantly occurs in G3, where secondary flows are present. However, in the real lung model, G4 also exhibits secondary flows, leading to particle deposition in this region. Furthermore, the length of G3 in the current segment of G3-G4 is shorter compared to G4, which contributes to less deposition in G3.

The deposition patterns of polydisperse fine and coarse particles (PM2.5, PM2.5–10) in relation to workplace pollutants are examined thoroughly using the idealized and real model. The patterns of total deposition of polydisperse particles (cumulative deposition across all particle diameters) at varying physical activity intensities in real lung model are presented in Fig. 12 for comparative study. Deposition rates of fine particles are lower compared to those of coarse particles. The lower deposition of fine particles can be attribute to their lower Stokes numbers, indicating their less inertial impact within the airways. For both fine and coarse particles, the deposition rates are observed to increase monotonically with rising levels of physical activity, reflecting enhanced particle transport and deposition under conditions of increased airflow and respiratory effort.

The difference in deposition efficiencies (DE) between fine and coarse particles becomes more pronounced with increasing physical activity. As activity levels intensify, the DE for coarse particles shows a steeper increase compared to fine particles, indicating a greater sensitivity to changes in activity intensity. This trend is supported by a linear curve fit using the least squares method for bituminous coal particles. The deposition efficiency for PM2.5 (fine particles) is represented by the equation $DE_{PM2.5} = 0.036PA + 0.66$, while for PM10 (coarse particles), it is $DE_{PM10} = 0.41PA + 4.14$. The steeper slope for PM10 confirms a more significant increase in deposition efficiency with higher physical activity levels compared to PM2.5, underscoring the greater impact of activity intensity on coarse particles.

The effect of gravity and secondary flows on deposition rates is evaluated through a comparative analysis utilizing the ideal lung model by including and then excluding the gravity term from the numerical model. The deposition rates of PM2.5–10 particles with and without the effects of gravity are shown in Fig. 13. When gravity was excluded, the DE dropped significantly and small differences in DE were observed at higher flow rates. The analysis indicates that the impact of gravity on deposition is more significant at lower flow rates and less significant at higher flow rates. Deposition in the post-bifurcation zone is governed entirely by gravity only (Figs. 14b and 15b).

In ideal lung model, expiratory deposition, in most cases, is observed at the top and bottom walls of parent branch but for higher flow rates and particle densities, it occurs on the side walls also. Convective deposition during exhalation requires the presence of strong secondary vortices and particles reaching the near wall with sufficient inertia to deposit [21]. At lower flow rates, flow remains laminar and secondary vortices are weak near the side walls, so particles do not deposit on the
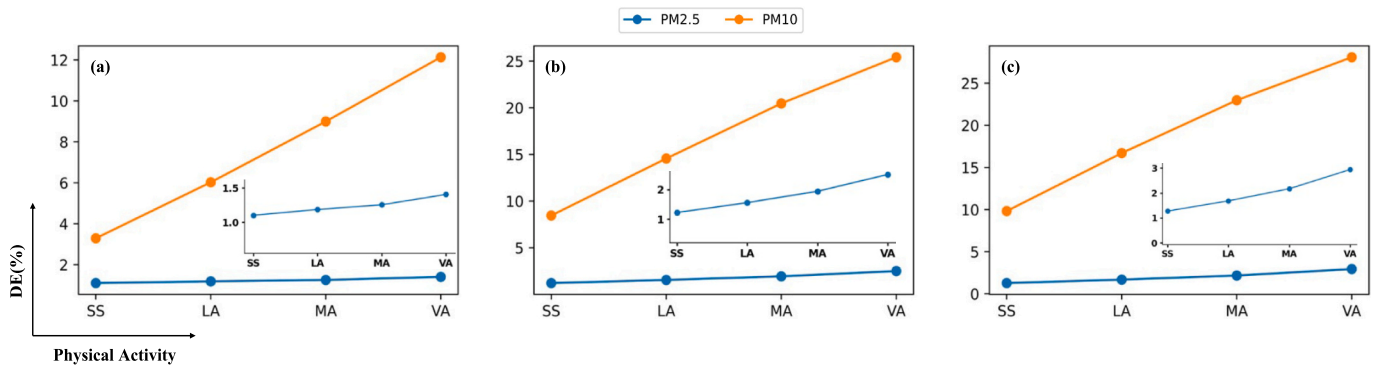
Fig. 12. Total deposition of polydisperse PM2.5 and PM2.5–10 particles for different pollutants - (a) Grain dust, (b) Coal fly ash, (c) Bituminous coal - in the real lung model.
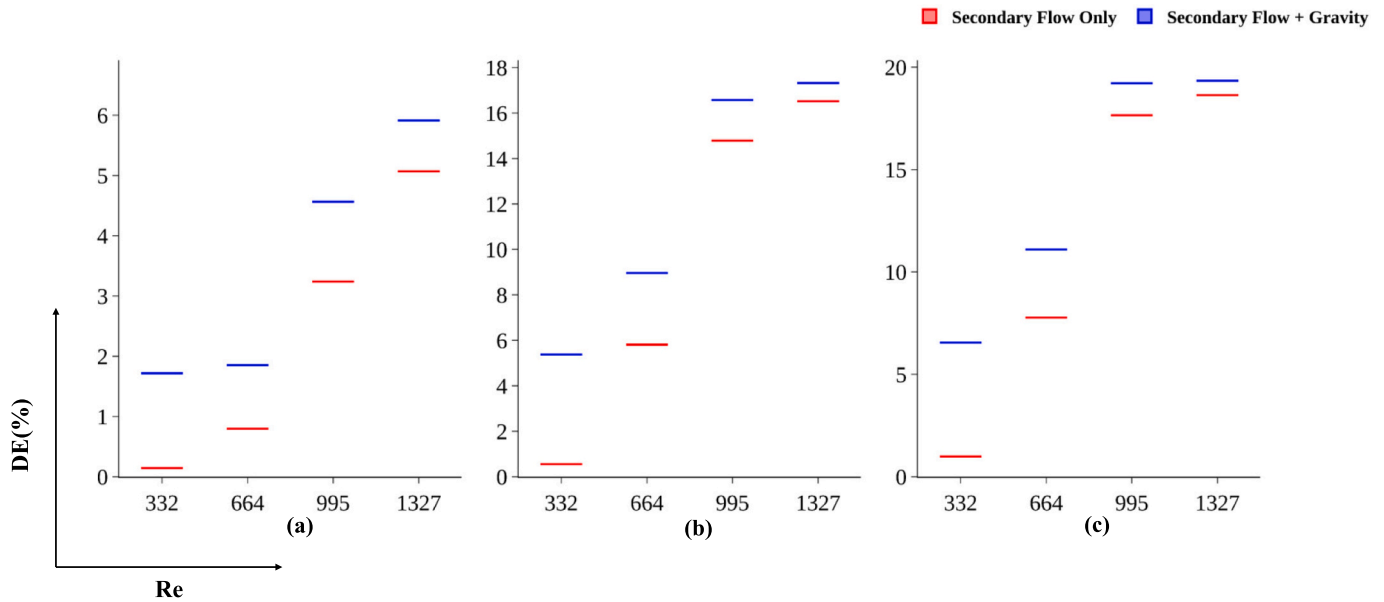

Fig. 13. Comparative analysis of impact of gravity on the deposition efficiency of polydisperse PM2.5–10 particles. Values along horizontal axis are the Reynolds numbers at G4 inlet. (a) GD, (b) CFA, (c) BC.

side walls irrespective of particle density and diameter (Fig. 15 side view). While at higher flow rates, transitional flow generated at the center of airway disperses the particles towards the airway walls and secondary-flow vortices become strong near the side walls. High density particles achieve enough inertia to deposit on the side walls driven by secondary-flow vortices (Fig. 15 side view). However lower density particles do not reach on side walls even at high flow rates because of low inertia (Fig. 14 side view).

In Fig. 16, deposition of polydisperse PM2.5–10 particles distribution is compared to that of two monodisperse distributions of constituent sizes of 5 μm and 10 μm using ideal lung model. The monodisperse particles of size 5 μm consistently exhibit a lower DE than the polydisperse particles whereas the DE of monodisperse 10 μm particles is significantly higher. The wide range of aerodynamic diameters in polydisperse distribution facilitates multiple deposition mechanisms resulting in higher deposition efficiencies (DEs) compared to those of smaller sized monodisperse distributions. The larger monodisperse particles (10 μm) have a greater DE due to their increased susceptibility to gravitational settling and inertial impaction. This analysis supports our hypothesis only for small-sized monodisperse distributions, highlighting that particle size distribution critically impacts deposition efficiencies during exhalation.

Fig. 17 and Fig. 18 illustrate the deposition patterns of individual

PM2.5 and PM2.5–10 particle diameters in polydisperse injection for ideal and real lung geometries, respectively. In the ideal lung model (Fig. 17), PM2.5 deposition is minimal, with the highest efficiency observed at 1.87 % for particles of 2.05 μm diameter, and no clear pattern emerges in the relationship between deposition efficiency and particle diameter. For all physical activity intensities, the deposition rate of 3.7 μm particles remains nearly the same within each particle density, though it varies across different densities. In Bituminous Coal and Coal Fly Ash particles, deposition efficiency curves for higher physical activity intensities (MA and VA) show significant overlap. A Similar overlap is observed in Grain Dust particles for the lower physical activity intensities (SS and LA).

In the real lung model (Fig. 18), PM2.5 deposition is more substantial, with only 1.15 μm particles exhibiting less than 1 % efficiency. Only grain dust particles in PM2.5 display some level of randomness in deposition efficiency. For PM2.5–10 particles, deposition efficiency rises with particle diameter and physical activity intensity. No overlap is observed in the deposition efficiency curves.

Fig. 19 offers a detailed examination of workplace pollutant deposition at different physical activity levels, considering a real lung model. The findings indicate that individuals involved in high-intensity activities, such as those in grain processing, coal mines, and fly ash brick industries, are prone to increased pollutant particle deposition. This
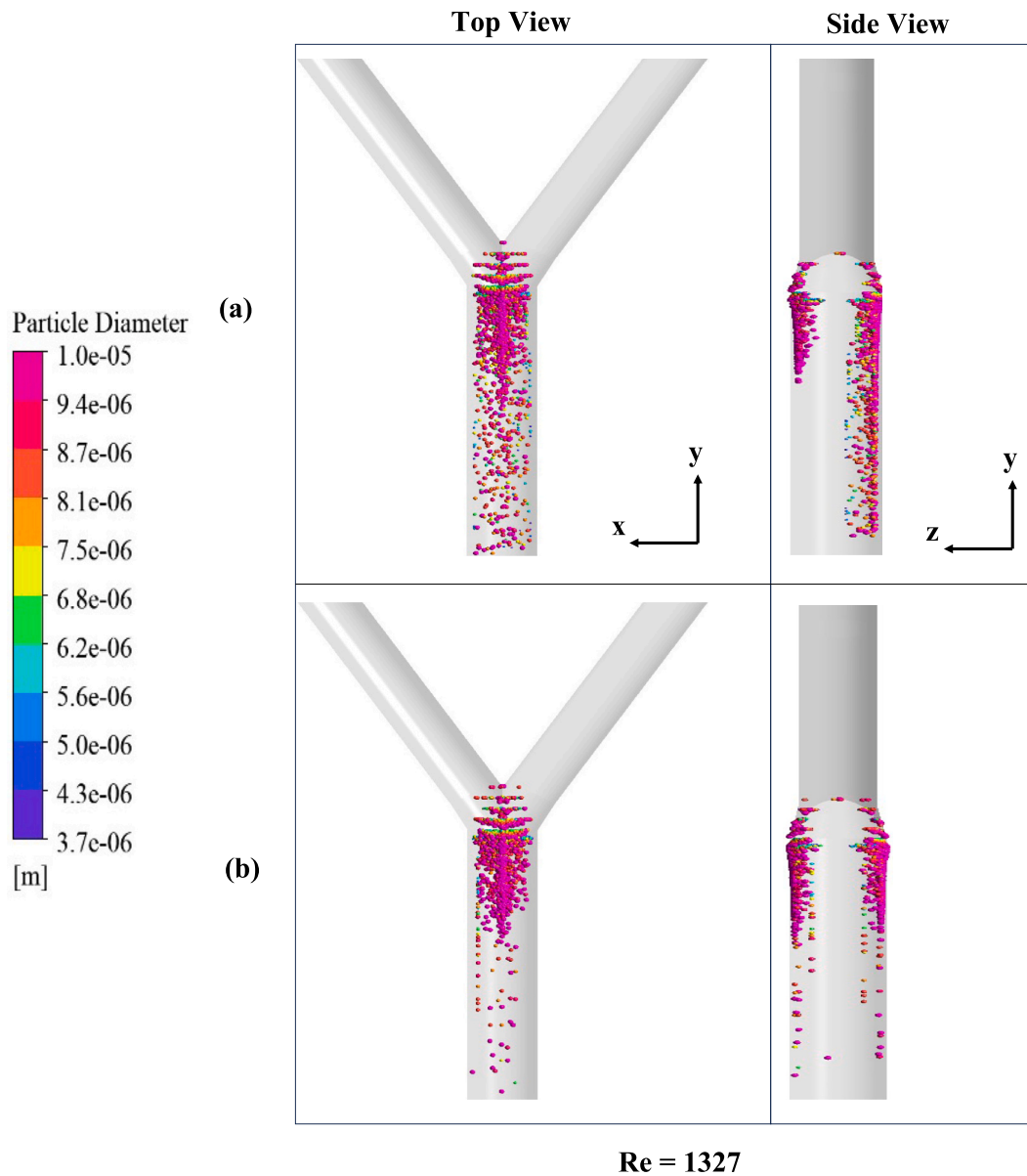
Fig. 14. Deposition patterns of polydisperse PM2.5–10 particles of GD at inlet Reynolds number 1327 for idealized model. (a) represents the combined effect of gravity and secondary flows on deposition. (b) represents the deposition due to secondary flows only.

heightened exposure in occupational settings raises concerns about potential risks of lung-related diseases.

4. Conclusion

A numerical study is performed on idealized and real models of airways G3-G4 to investigate the deposition patterns of fine (PM2.5) and coarse (PM2.5–10) polydisperse particles during exhalation. The effects of varying levels of physical activity on the deposition of pollutant particles of grain dust, coal fly ash, and bituminous coal are studied. Deposition trends of mono and polydisperse particles are also compared. Key findings from the study include:

- In the real airway model, anatomical complexities lead to an early emergence of secondary flows, whereas in the idealized model, these secondary flows occur after the flow passes the cranial ridge.

- A notable shift in deposition patterns from pre- to post-bifurcation zones is observed in the real model compared to the idealized model.
- During inhalation, deposition primarily occurs near the cranial ridge due to inertial impaction, while exhalation results in deposition shifting to the pre- and post-bifurcation zones.
- The effect of gravity on deposition, compared to secondary flow, is more pronounced at lower flow rates but diminishes at higher flow rates.
- PM2.5 deposition is minimal and random in the idealized model but becomes more significant and consistent in the real model. Substantial deposition rates are observed for PM2.5–10 particles.
- Deposition of particles of grain dust, fly ash, and coal particles has a direct relation with the intensity of PA.

While existing scientific literature has explored inspiratory deposition, a significant gap persists in understanding expiratory deposition. The present study contributes to addressing this gap because an in-depth
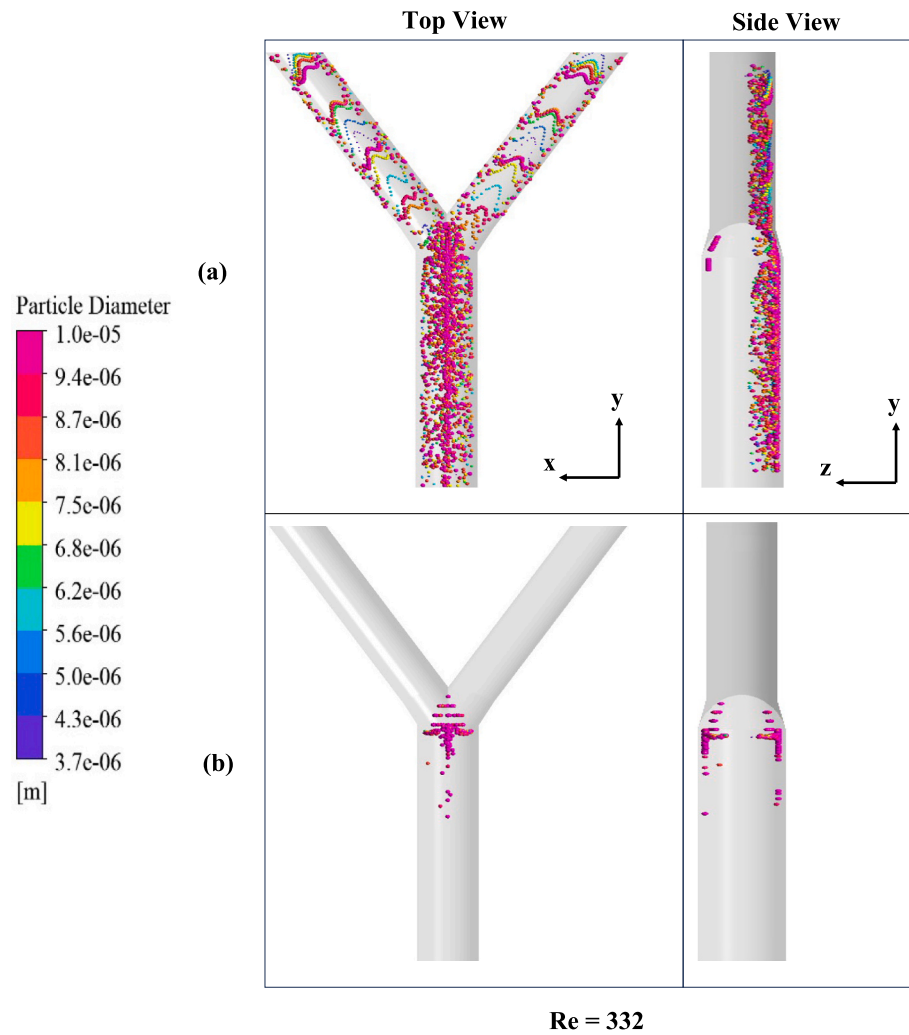
Fig. 15. Deposition patterns of polydisperse PM2.5–10 particles of BC at inlet Reynolds number 332 for idealized model. (a) represents the combined effect of gravity and secondary flows on deposition. (b) represents the deposition due to secondary flows only.
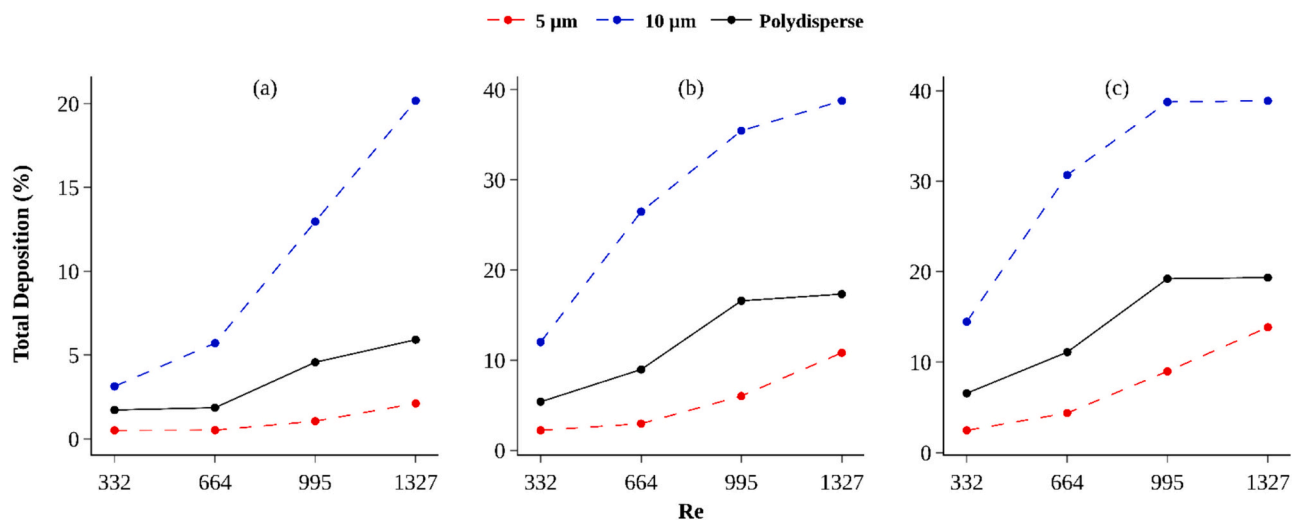

Fig. 16. Total deposition comparison of mono and polydisperse particles with reference to inlet Reynolds numbers for idealized model, (a): GD, (b): CFA, (c): BC.
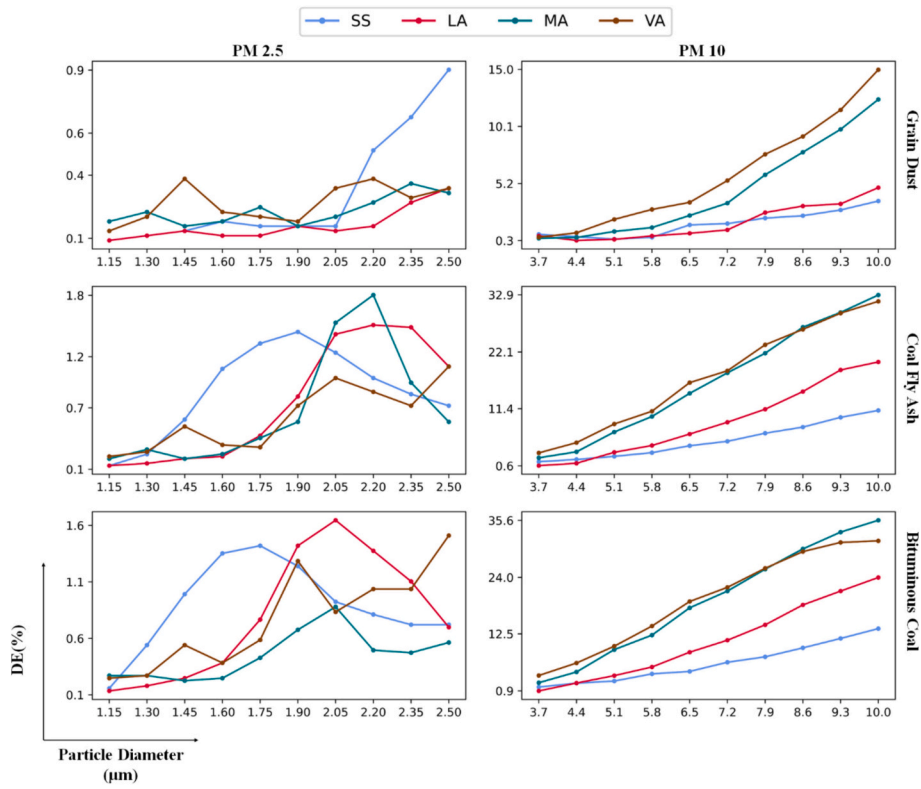
Fig. 17. Deposition of individual particle diameters based on their initial distributions (Ideal lung model).
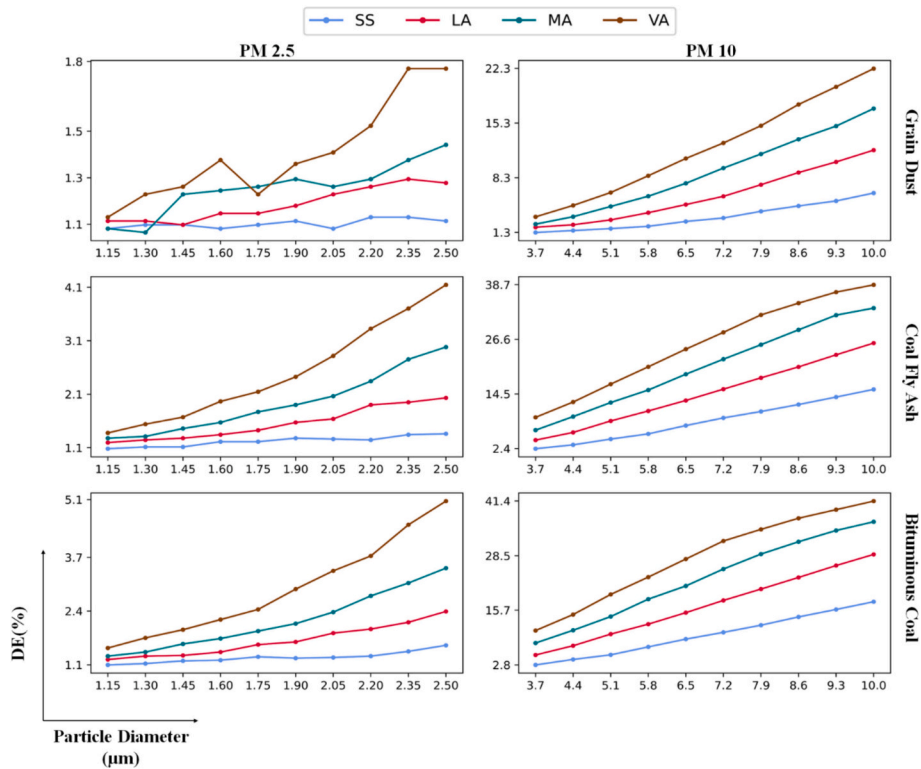

Fig. 18. Deposition of individual particle diameters based on their initial distributions (Real lung model).

Fig. 19. Deposition efficiency (%) trends of PM2.5 and PM2.5–10 particles in relation to physical activity intensity and pollutant type (Realistic G3-G4 airway model).

analysis of exhalation-driven deposition is essential to understanding complete deposition patterns in polluted environments. Our focus has been on a single bifurcation; however, future investigations will extend to multiple generations of the real lung model to provide a more comprehensive analysis.

CRediT authorship contribution statement

Muhammad Farrukh Mehmood: Writing – original draft, Visualization, Validation, Methodology, Investigation, Formal analysis, Data curation. **Adnan Munir:** Writing – original draft, Supervision, Project administration, Methodology, Conceptualization. **Umar Farooq:** Visualization, Validation, Methodology, Investigation. **Hafiz Hamza Riaz:** Writing – review & editing, Visualization, Methodology, Formal analysis. **Ming Zhao:** Writing – review & editing, Supervision, Project administration. **Mohammad S. Islam:** Writing – review & editing, Supervision, Project administration.

Declaration of competing interest

The authors declare that they have no known competing financial interests or personal relationships that could have appeared to influence the work reported in this paper.

Data availability

Data will be made available on request.

References

[1] Ansys Fluent User''s Guide. http://www.ansys.com, 2022.
[2] I. Balásházy, W. Hofmann, Particle deposition in airway bifurcations–II. Expiratory flow, J. Aerosol Sci. 24 (6) (1993) 773–786, https://doi.org/10.1016/0021-8502(93)90045-B.
[3] M. Biglarian, M. MomeniLarimi, B. Firoozabadi, K. Inthavong, A. Farnoud, Targeted drug delivery with polydisperse particle transport and deposition in patient-specific upper airway during inhalation and exhalation, Respir. Physiol. Neurobiol. 308 (2023) 103986, https://doi.org/10.1016/j.resp.2022.103986.
[4] M. de Guadalupe Vargas Canto, J.G.C. Bretón, A.A.E. Guzmán, R.M.C. Bretón, C. Guarnaccia, Health risk assessment due to inhalation of heavy metals in PM10 in urban ambient air in San Francisco De Campeche, Campeche, AIP Conf. Proc. 3084 (1) (2024) 70001, https://doi.org/10.1063/5.0199586.
[5] X.G. Cui, E.M. Littringer, N.A. Urbanetz, E. Gutheil, Large eddy simulation of polydisperse particle deposition in an idealized mouth-throat, Atomiz. Sprays 28 (2) (2018) 179–193, https://doi.org/10.1615/AtomizSpr.2018025127.

[6] Q. Deng, C. Ou, Y.-M. Shen, Y. Xiang, Y. Miao, Y. Li, Health effects of physical activity as predicted by particle deposition in the human respiratory tract, Sci. Total Environ. 657 (2019) 819–826, https://doi.org/10.1016/j.scitotenv.2018.12.067.
[7] S. Feng, Y. Li, Study on coal fly ash classified by bulk density, J. Phys. Conf. Ser. 1732 (1) (2021) 012127, https://doi.org/10.1088/1742-6596/1732/1/012127.
[8] S. Gautam, A.K. Patra, S.P. Sahu, M. Hitch, Particulate matter pollution in opencast coal mining areas: a threat to human health and environment, Int. J. Min. Reclam. Environ. 32 (2) (2018) 75–92, https://doi.org/10.1080/17480930.2016.1218110.
[9] A.D. Gosman, E. Loannides, Aspects of computer simulation of liquid-fueled combustors, J. Energy 7 (6) (1983) 482–490, https://doi.org/10.2514/3.62687.
[10] N. Gupta, V.V. Gedam, C. Moghe, P. Labhasetwar, Investigation of characteristics and leaching behavior of coal fly ash, coal fly ash bricks and clay bricks, Environ. Technol. Innov. 7 (2017) 152–159, https://doi.org/10.1016/j.eti.2017.02.002.
[11] O. Hahad, A. Daiber, T. Münzel, Physical activity in polluted air: an urgent call to study the health risks, Lancet Planet. Health 7 (4) (2023) e266–e267, https://doi.org/10.1016/S2542-5196(23)00055-4.
[12] O. Hahad, M. Kuntic, K. Frenis, S. Chowdhury, J. Lelieveld, K. Lieb, A. Daiber, T. Münzel, Physical activity in polluted air—net benefit or harm to cardiovascular health? A comprehensive review, Antioxidants 10 (11) (2021) 1787, https://doi.org/10.3390/antiox10111787.
[13] W. Hofmann, Modelling inhaled particle deposition in the human lung—a review, J. Aerosol Sci. 42 (10) (2011) 693–724, https://doi.org/10.1016/j.jaerosci.2011.05.007.
[14] K. Inthavong, L.-T. Choi, J. Tu, S. Ding, F. Thien, Micron particle deposition in a tracheobronchial airway model under different breathing conditions, Med. Eng. Phys. 32 (10) (2010) 1198–1212, https://doi.org/10.1016/j.medengphy.2010.08.012.
[15] M.S. Islam, S.C. Saha, T. Gemci, I.A. Yang, E. Sauret, Y.T. Gu, Polydisperse microparticle transport and deposition to the terminal bronchioles in a heterogeneous vasculature tree, Sci. Rep. 8 (1) (2018) 16387, https://doi.org/10.1038/s41598-018-34804-x.
[16] M.S. Islam, S.C. Saha, T. Gemci, I.A. Yang, E. Sauret, Z. Ristovski, Y.T. Gu, Euler-lagrange prediction of diesel-exhaust polydisperse particle transport and deposition in lung: anatomy and turbulence effects, Sci. Rep. 9 (1) (2019) 12423, https://doi.org/10.1038/s41598-019-48753-6.
[17] K. Iyogun, S.A. Lateef, G.R.E.E. Ana, Lung function of grain millers exposed to grain dust and diesel exhaust in two food markets in ibadan metropolis, Nigeria, Saf. Health Work 10 (1) (2019) 47–53, https://doi.org/10.1016/j.shaw.2018.01.002.
[18] N.A.H. Janssen, P. Fischer, M. Marra, C. Ameling, F.R. Cassee, Short-term effects of PM2.5, PM10 and PM2.5–10 on daily mortality in the Netherlands, Sci. Total Environ. 463–464 (2013) 20–26, https://doi.org/10.1016/j.scitotenv.2013.05.062.
[19] C.S. Kim, A.J. Iglesias, L. Garcia, Deposition of inhaled particles in bifurcating airway models: II. Expiratory deposition, J. Aerosol. Med. 2 (1) (1989) 15–27, https://doi.org/10.1089/jam.1989.2.15.
[20] A. Li, G. Ahmadi, Dispersion and deposition of spherical particles from point sources in a turbulent channel flow, Aerosol Sci. Technol. 16 (4) (1992) 209–226, https://doi.org/10.1080/02786829208959550.
[21] P.W. Longest, S. Vinchurkar, Inertial deposition of aerosols in bifurcating models during steady expiratory flow, J. Aerosol Sci. 40 (4) (2009) 370–378, https://doi.org/10.1016/j.jaerosci.2008.11.007.
[22] P.W. Longest, S. Vinchurkar, T. Martonen, Transport and deposition of respiratory aerosols in models of childhood asthma, J. Aerosol Sci. 37 (10) (2006) 1234–1257, https://doi.org/10.1016/j.jaerosci.2006.01.011.
[23] F. Lu, D. Xu, Y. Cheng, S. Dong, C. Guo, X. Jiang, X. Zheng, Systematic review and meta-analysis of the adverse health effects of ambient PM2.5 and PM10 pollution in the Chinese population, Environ. Res. 136 (2015) 196–204, https://doi.org/10.1016/j.envres.2014.06.029.
[24] D. Luo, Z.V. Luo, X. Zheng, H. Qian, Beyond droplet deposition: virus transport and deposition modeling in respiratory tract influenced by ambient environment and exhalation activities, Build. Environ. 255 (2024) 111406, https://doi.org/10.1016/j.buildenv.2024.111406.
[25] G. Morantes, J.C. González, G. Rincón, Characterisation of particulate matter and identification of emission sources in Greater Caracas, Venezuela, Air Qual. Atmos. Health 14 (12) (2021) 1989–2014, https://doi.org/10.1007/s11869-021-01070-2.
[26] C.J. Musante, J.D. Schroeter, J.A. Rosati, T.M. Crowder, A.J. Hickey, T. B. Martonen, Factors affecting the deposition of inhaled porous drug particles, J. Pharm. Sci. 91 (7) (2002) 1590–1600, https://doi.org/10.1002/jps.10152.
[27] C. Nishida, K. Yatera, The impact of ambient environmental and occupational pollution on respiratory diseases, Int. J. Environ. Res. Public Health 19 (5) (2022), https://doi.org/10.3390/ijerph19052788.
[28] R. Paul, O. Adeyemi, A.A. Arif, Estimating mortality from coal workers' pneumoconiosis among Medicare beneficiaries with pneumoconiosis using binary regressions for spatially sparse data, Am. J. Ind. Med. 65 (4) (2022) 262–267, https://doi.org/10.1002/ajim.23330.
[29] O. Pourmehran, B. Cazzolato, Z. Tian, M. Arjomandi, Acoustically-driven drug delivery to maxillary sinuses: aero-acoustic analysis, Eur. J. Pharm. Sci. 151 (2020) 105398, https://doi.org/10.1016/j.ejps.2020.105398.
[30] O. Pourmehran, T.B. Gorji, M. Gorji-Bandpy, Magnetic drug targeting through a realistic model of human tracheobronchial airways using computational fluid and particle dynamics, Biomech. Model. Mechanobiol. 15 (5) (2016) 1355–1374, https://doi.org/10.1007/s10237-016-0768-3.
[31] O. Pourmehran, M. Rahimi-Gorji, M. Gorji-Bandpy, T.B. Gorji, Simulation of magnetic drug targeting through tracheobronchial airways in the presence of an

external non-uniform magnetic field using Lagrangian magnetic particle tracking, J. Magn. Magn. Mater. 393 (2015) 380–393, https://doi.org/10.1016/j.jmmm.2015.05.086.

[32] K. Pradhan, A. Guha, Fluid dynamics of a bifurcation, Int. J. Heat Fluid Flow 80 (2019) 108483, https://doi.org/10.1016/j.ijheatfluidflow.2019.108483.

[33] S. Quirce, A. Diaz-Perales, Diagnosis and management of grain-induced asthma, Allergy, Asthma Immunol. Res. 5 (6) (2013) 348–356, https://doi.org/10.4168/aair.2013.5.6.348.

[34] M. Rahman, M. Zhao, M.S. Islam, K. Dong, S.C. Saha, Numerical study of nano and micro pollutant particle transport and deposition in realistic human lung airways, Powder Technol. 402 (2022) 117364, https://doi.org/10.1016/j.powtec.2022.117364.

[35] H.H. Riaz, A.H. Lodhi, A. Munir, M. Zhao, U. Farooq, M.N.M. Qadri, M.S. Islam, Breathing in danger: mapping microplastic migration in the human respiratory system, Phys. Fluids 36 (4) (2024) 43338, https://doi.org/10.1063/5.0205303.

[36] K.A. Rosentrater, R. Bucklin, Chapter 6 - Structural, physical, and engineering properties of cereal grains and grain products, in: K.A. Rosentrater (Ed.), Storage of Cereal Grains and Their Products, Fifth edition, Woodhead Publishing, 2022, pp. 135–178, https://doi.org/10.1016/B978-0-12-812758-2.00019-2.

[37] E.M. Saber, G. Heydari, Flow patterns and deposition fraction of particles in the range of 0.1–10μm at trachea and the first third generations under different breathing conditions, Comput. Biol. Med. 42 (5) (2012) 631–638, https://doi.org/10.1016/j.compbiomed.2012.03.002.

[38] P.G. Saffman, The lift on a small sphere in a slow shear flow, J. Fluid Mech. 22 (2) (1965) 385–400, https://doi.org/10.1017/S0022112065000824.

[39] R. Tambun, K. Furukawa, M. Hirayama, M. Shimadzu, S. Yamanaka, Y. Ohira, Measurement and estimation of the particle size distribution by the Buoyancy Weighing-Bar method and the Rosin-Rammler equation, J. Chem. Eng. Japan 49 (2) (2016) 229–233, https://doi.org/10.1252/jcej.14we129.

[40] P. Thakur, Chapter 5 - Pore pressure and stress field in coal reservoirs, in: P. Thakur (Ed.), Advanced Reservoir and Production Engineering for Coal Bed Methane, Gulf Professional Publishing, 2017, pp. 61–73, https://doi.org/10.1016/B978-0-12-803095-0.00005-3.

[41] O. Vandenplas, Occupational asthma: etiologies and risk factors, Allergy, Asthma Immunol. Res. 3 (3) (2011) 157, https://doi.org/10.4168/aair.2011.3.3.157.

[42] L.G. Vargas Buonfiglio, I.A. Mudunkotuwa, M.H. Abou Alaiwa, O.G. Vanegas Calderón, J.A. Borcherding, A.K. Gerke, J. Zabner, V.H. Grassian, A.P. Comellas, Effects of coal fly ash particulate matter on the antimicrobial activity of airway surface liquid, Environ. Health Perspect. 125 (7) (2017), https://doi.org/10.1289/EHP876.

[43] E.R. Weibel, Morphometry of the Human Lung, Springer Berlin Heidelberg, 1963, https://doi.org/10.1007/978-3-642-87553-3.

[44] World Health Organization, Air Pollution, 2023.

[45] Ł. Zaręba, K. Piszczatowska, K. Dżaman, K. Soroczynska, P. Motamedi, M.J. Szczepański, N. Ludwig, The relationship between fine particle matter (PM2.5) exposure and upper respiratory tract diseases, J. Personal. Med. 14 (1) (2024), https://doi.org/10.3390/jpm14010098.

[46] Z. Zhang, C. Kleinstreuer, J.F. Donohue, C.S. Kim, Comparison of micro- and nano-size particle depositions in a human upper airway model, J. Aerosol Sci. 36 (2) (2005) 211–233, https://doi.org/10.1016/j.jaerosci.2004.08.006.

[47] G. Zhou, Z. Liu, W. Shao, B. Sun, L. Li, J. Liu, G. Li, X. Lv, Study on the effects of dust particle size and respiratory intensity on the pattern of respiratory particle deposition in humans, Indoor Air 2024 (1) (2024) 5025616, https://doi.org/10.1155/2024/5025616.

[48] K.M. Zierold, C. Odoh, A review on fly ash from coal-fired power plants: chemical composition, regulations, and health evidence, Rev. Environ. Health 35 (4) (2020) 401–418, https://doi.org/10.1515/reveh-2019-0039.